Robotic Fast Cell Positioning Based on a Narrow-Necked Micropipette in Cell Transportation

Shaojie Fu, Jinyu Qiu, Ruimin Li, Biting Ma, Mengya Liu, Hao Chen,
Mingzhu Sun, *Member, IEEE*, Xin Zhao, *Member, IEEE*, and Qili Zhao, *Member, IEEE*

***Abstract*—In this article, a narrow-necked micropipette (NNM) was designed, fabricated, and utilized for robotic fast cell positioning in cell transportation. First, key geometrical parameters of NNM were determined through the aspiration model and computational microfluidics model. Then, a heating-and-rotation method was developed to fabricate a narrow neck structure inside the micropipette based on a heating model. Further, the dynamic models of the cell before and after being held by the narrow neck were conducted. Based on that, a sliding mode motion controller and a deformation controller were designed for fast positioning of the cell at the narrow neck position and reducing the cell deformation, respectively. Robotic transportation results of 15 sheep oocytes demonstrate that our system can position the cell with a 100% success rate at doubled throughput in comparison to the traditional methods. The average positioning error and cell deformation degree are significantly reduced to 1.89 pixels and 2.59%, respectively. In addition, experiments on HeLa cells showed an average position time of 2.1 s with 100% success rate. Besides, limited harm to the cell survival rate is found through culturing experiments. With the above advantages, our robotic system is expected to improve cell transportation efficiency in the future.**

Received 8 October 2025; accepted 23 March 2026. Recommended by Technical Editor Y. Cha and Senior Editor K. Oldham. This work was supported in part by the National Natural Science Foundation of China under Grant 62273186 and Grant 62333012, in part by the Guangdong Basic and Applied Basic Research Foundation under Grant 2024A1515011171, and in part by Shenzhen Science and Technology Program under Grant JCYJ20250604185817023. *(Corresponding author: Qili Zhao.)*

The authors are with the Institute of Robotics and Automatic Information System (IRAIS), the Tianjin Key Laboratory of Intelligent Robotic (tjKLIR), Nankai University, Tianjin 300071, China, also with the Engineering Research Center of Trusted Behavior Intelligence Ministry of Education, Nankai University, Tianjin 300071, China, also with the Institute of Intelligence Technology and Robotic Systems, Shenzhen Research Institute of Nankai University, Shenzhen 518083, China, and also with the National Key Laboratory of Intelligent Tracking and Forecasting for Infectious Diseases, Nankai University, Tianjin 300071, China (e-mail: fushaojie@mail.nankai.edu.cn; qiujinyu@mail.nankai.edu.cn; lrumin@163.com; mabiting@mail.nankai.edu.cn; liumengya@mail.nankai.edu.cn; 1120240271@mail.nankai.edu.cn; sunmz@nankai.edu.cn; zhaoxin@nankai.edu.cn; zhaoqili@nankai.edu.cn).

This article has supplementary material provided by the authors and color versions of one or more figures available at https://doi.org/10.1109/TMECH.2026.3678739.

Digital Object Identifier 10.1109/TMECH.2026.3678739

***Index Terms*—Automated cell manipulation, microoperation, robotic cell positioning, robotic cell transportation operation.**

I. INTRODUCTION

CELL transportation, pick-and-place the cell among different culture medium droplets, is a key step in many biological and medical applications, such as cell vitrification [1], [2], cell washing during culture processes [3], cell pairing manipulation [4], [5], single-cell analyses [6], [7], disease detection based on cell state [8], tumor cell detection [9], mechanical and electrical characterization of cells [10] et al. Current cell transportation tools include optical tweezers [11], [12], [13], microfluidic devices [14], [15], dielectrophoresis [16], [17], microgrippers [18], and micropipettes [19], [20], [21], [22], [23]. Among them, the micropipette is most widely used in cell transportation due to its easy availability and no additional equipment requirements.

The key step in cell transportation based on a micropipette is the cell positioning inside the micropipette, in which the operator aspirates a target cell into a micropipette and then positions it to a designated position close to the micropipette opening, as shown in Fig. 1(a). In this way, the cell is kept in the field of view during whole-cell transportation. More importantly, the amount of liquid from the old culture medium droplet being injected into the new droplet during placing the cell can be limited to reduce the contamination incidences to the new droplet. As a lack of structure inside the common straight micropipette (CSM) to stop and hold the cell by force, the operators usually manually adjust the aspirating pressure to conduct the cell positioning task inside the CSM. Due to the small volume and light weight of a single cell, the cell moves easily even under small pressure disturbances. Thus, the operators need to carefully adjust the air pressure repetitively based on the position of the cell inside the CSM with trial and error, which usually requires high operation experience and long operation time, significantly limiting the broad application of cell positioning in cell transportation. In response to the problems of manual operation, automated cell positioning technologies inside CSM have been developed in recent years. For example, Zhang et al. proposed a single sperm aspirating and positioning technique based on a CSM

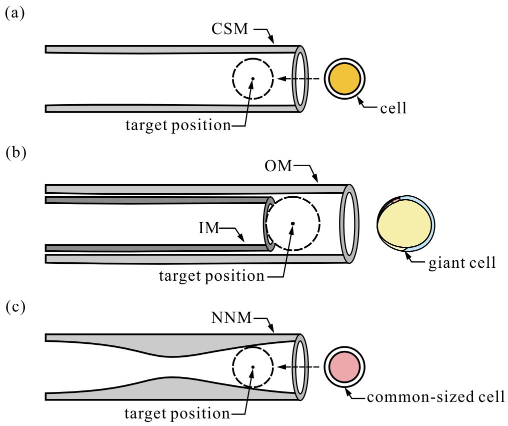

Fig. 1. Schematic: Cell positioning methods based on different kinds of micropipettes. (a) Common straight micropipette (CSM). (b) Bilayer micropipette. (c) Our proposed narrow-necked micropipette (NNM).

and achieved closed-loop robust control of sperm dynamics [20]. Shan et al. [21] considered the compressibility and deformation of oil and proposed a cell aspiration model based on an oil-driven pump, then designed an adaptive controller for cell positioning. Zhao et al. [22] used an air pump integrating an ADRC controller to control cell movement for precise cell positioning in a CSM. Zhang et al. [2] modeled the dynamics of embryo motion and developed a linear quadratic regulator controller to pick multiple embryos one by one into the CSM for embryo vitrification. The traditional cell transportation methods based on CSM usually need to conduct the cell positioning task by repeated adjustment of aspiration pressure, due to a lack of structure inside CSM to stop the cell by force, which usually costs some time.

Using a CSM with an opening diameter smaller than the cell size to hold the cell with its opening can conduct cell positioning tasks by force in a short time. However, in that way, part of the cell surface needs to be exposed to the oil or air environment while the CSM with the cell moves from one droplet to another. However, in that way, part of the cell surface needs to be exposed out of CSM opening. While the CSM with the cell moves out of the droplet during transportation, the held cell may be pulled off the CSM by the significant force generated at the interface between the droplet and oil environment covering it. To keep the cell and meanwhile conduct the cell positioning task, a new narrow-necked micropipette (NNM) with a large opening diameter and a small inner diameter inside the CSM is required for aspiration of the cell with its large opening and to hold it with the narrow-neck structure inside. In previous research, we developed a bilayer micropipette made by inserting a thin glass micropipette into a thick one [24] as shown in Fig. 1(b), which aspirates a cell into the opening of the outer micropipette (OM) and holds the cell with the opening of the inside micropipette (IM). However, to reduce the pressure leakage through the gap between the two micropipettes, the outer diameter of the IM needs to be close to the inner diameter of the OM. The above requirement significantly increases the challenge in assembling the bilayer micropipette when inserting the thin micropipette into the thicker one, easily leading to a crush between them. To prevent the break of them in the crush, the two micropipettes need to be thick enough to guarantee enough strengths. For example, the IM in the previous studies had to choose the commercial glass micropipette with a 1 mm outer diameter and an inner diameter of 800 μm, making it only capable of holding special giant cells with a diameter larger than 800 μm, such as zebrafish embryos. For common domestic oocytes and somatic cells with much smaller sizes, the above bilayer micropipette is not suitable for transporting them. Besides lacking an appropriate NNM, the deformation of the held cell needs to be limited to reduce the mechanical harm to the cell during the cell-holding process. In summary, a new thinner NNM with a cell deformation control method is required for the transportation of common-sized cells and reducing mechanical damage to them.

This article developed a robotic fast cell positioning method for transportation of common-sized cells based on a self-developed NNM as shown in Fig. 1(c). First, the key geometrical parameters of the NNM were determined through the aspiration model and computational microfluidics model. Then, a heating-and-rotation method was developed to fabricate a narrow-necked structure inside the CSM based on force analysis and a developed heating model. Further, dynamic models of the cell before and after being held by the narrow neck were carried out based on fluidic simulation and force analysis, respectively. Furthermore, a sliding mode controller combined with cell position feedback was designed to accelerate the cell positioning process before the cell is held. Finally, a cell deformation controller was designed to reduce the mechanical damage to cells after it is held by the narrow neck. The NNM fabrication results demonstrate that the proposed fabrication method can make the narrow neck structure with inner diameter errors of less than 1.23% and position variations below 1.28%, showing a good repeatability of the fabricated narrow neck structure. The experimental results of 15 sheep oocytes demonstrate that the method can position the cells at the narrow neck position in an average of 1.06 seconds, which is a doubled throughput of the traditional methods, with a 100% operation success rate, a positioning error of 1.89 pixels and 2.59% cell deformation degree on average (versus 5.34 pixels and 6.34% of manual positioning results using NNM). In addition, experiments with 30 HeLa cells showed an average positioning time of 2.1 s, which is a triple throughput of the traditional methods. The cross-droplet transportation of HeLa cells was tested, and the success rate based on robotic NNM was as high as 100% (vs. manual NNM 83.3% and manual CSM 53.3%). Oocyte culturing results demonstrate a 100% oocyte survival rate after being operated on by the proposed system, compared with an 81.3% survival rate of the manual cell transportation method using NNM. HeLa cells culturing results demonstrate a 100% survival rate (versus manual NNM 84%). With the above advantages, the proposed robotic cell positioning method is expected to improve cell transportation efficiency in the future.

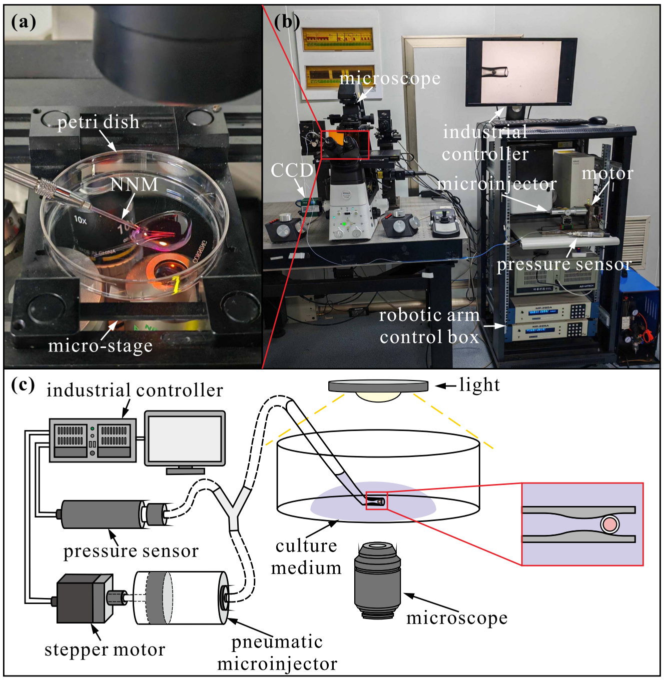

Fig. 2. Photo and schematic of robotic cell positioning system for cell transportation. (a) Partial enlarged view of the Petri dish. (b) System photo Schematic. (c) Schematic: robotic cell transportation system based on NNM.

II. System Setup

The robotic cell positioning system for cell transportation in this article is built within the laboratory [22] as shown in Fig. 2. The system is conducted based on an inverted microscope (Nikon, Eclipse TI-E, Japan) with a CCD camera (Balser, acA645-100gm, Germany) integrated into it to capture microscopic images at 50 frames/second with a resolution of 640 × 480 pixels. An X-Y microstage (Prior, ProScan III, U.K.) with a motion range of 120 mm × 80 mm and a positioning resolution of 0.05 μm is equipped to place and position the petri dish culturing cells. In addition, an X-Y-Z micromanipulator (Sutter, MP285, USA) with a motion range of 25 mm × 25 mm × 25 mm and a positioning resolution of 0.04 μm is equipped to mount an NNM for cell positioning. A pneumatic microinjector (Narishige, IM-11-2, Japan) with a pressure variation range of about -200 to 200 hPa is utilized to provide the pressure inside the micropipette for cell positioning. A stepper motor (Hanpose, 42BYGP40-G19, China) with a motor driver (Vince, VSMD103, China) is used to control the motion of the piston of the pneumatic microinjector and thereby adjust the pressure for cell position. A host computer is in charge of image processing, motion control of the microstage and micromanipulators, and pressure control of the air pump.

III. Key Technologies and Methodologies

A novel NNM is designed and fabricated in this section for achieving a fast cell positioning task in cell transportation. Then, the dynamic models of the cell before and after it is held by the narrow neck are conducted for the following positioning control. Based on the above work, a sliding mode controller and a cell deformation controller are designed for fast positioning of the cell and reducing the cell deformation after it is held by the narrow neck, respectively.

A. Key Geometrical Parameters Determination for NNM Based on Aspiration Model and Microfluidic Model

The key geometrical parameters of the NNM needing to be determined include the diameter of the micropipette opening D_o, the inner diameters of the narrow neck D_n, and the distance between the opening and narrow neck L_d.

The opening inner diameter D_o is determined by the size of the target cell types, which is slightly larger than the size of the target cell. In comparison, the determination process of inner diameter D_n at the narrow neck position is rather complicated. The narrow neck inner diameter should be neither too large to hold the cell nor too small to generate enough aspiration force to aspirate the cell into its opening or generate a steady flow inside the micropipette for precise cell positioning. Thus, an appropriate range of the inner diameter of the micropipette at the narrow neck position needs to be determined.

When the length of the narrow neck structure is significantly longer than the cell size, the narrow neck position can be simplified as a local thin micropipette inside the thick micropipette. According to the aspiration model of our previous research [24], the maximum inner diameters of the narrow neck part required for holding the spherical solidlike cells can be determined according to the aspiration model as

$$R_{Pmax} = \sqrt[3]{\frac{8\pi E r_c^3}{9\Phi P_{Amax} - 4\pi E}} \tag{1}$$

where R_{Pmax} is the maximum value of narrow neck radius, E is the Young's modulus of the cell, r_c is the radius of the cell, Φ is a term that depends weakly on the ratio of the thickness of the pipette wall to the radius of the pipette. A typical value for $\Phi \approx 2.1$. P_{Amax} is the maximum value of aspiration pressure that the pump provides. The reader may find details of the cell aspiration model in Section I of the supplementary file "Supplementary file.pdf" or our previous paper [24].

To determine the minimum appropriate inner diameter of the narrow neck D_n, the microfluidic fields inside and outside of the micropipette are simulated based on a computational microfluidic model. The detailed introduction of the computational microfluidics model is given in Section II of the uploaded supplementary file "Supplementary file.pdf". The geometrical model of the micropipette is determined according to the observation results of the made NNM. The aspiration pressure inside NNM is set to be consistent with that required for aspiration of the cell into the CSM with the same opening inner diameter. For aspiration of sheep oocytes in the MII stage, the inner diameter of the micropipette opening and required aspiration velocity are set as 200 μm and 0.1 mm/s, respectively, according to experiments. The obtained microfluidic fields of NNM compared to those of the CSMs are shown in Fig. 3, and a larger range of simulation results is shown in Fig. S2.

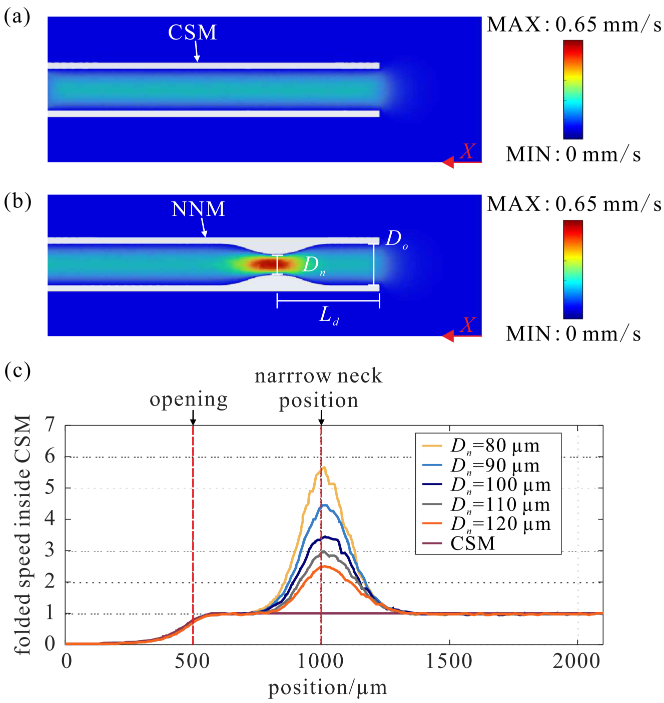

Fig. 3. Computational microfluidic model inside and outside of NNM. (a) Computational fluid dynamics simulation results in a CSM when the aspiration velocity at the inlet wall is 0.1 mm/s. (b) Computational fluid dynamics simulation results in an NNM when the aspiration velocity at the inlet wall is 0.1 mm/s. (c) Liquid velocity curve in the X-axis direction (straight micropipette and $d_m = 80$–120 μm, step size is 10 μm).

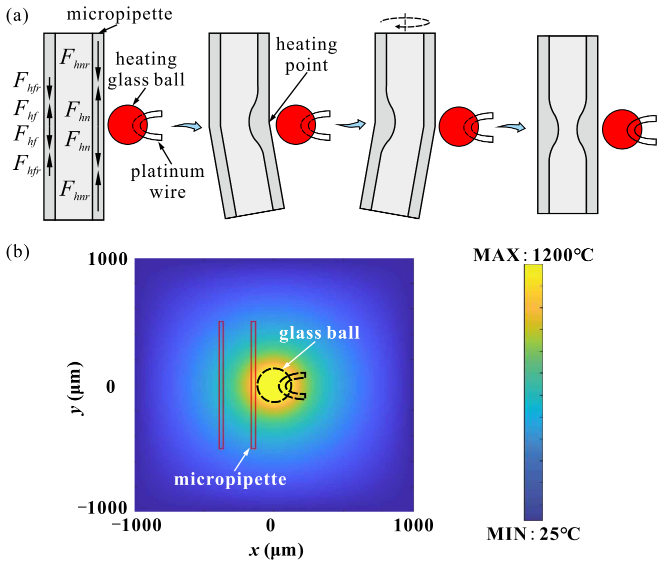

Fig. 4. The fabrication process of NNM based on force analysis and the heating-and-rotation method. (a) Force analysis of the micropipette during the heating process and bending the micropipette on a side by heating with a glass ball embedded with a platinum wire. Then the micropipette rotated by 180° and was heated at the other side, thereby causing a depression in the middle of the micropipette. (b) Temperature field obtained by Thermal Diffusion Equation model.

It can be found that the existence of the narrow neck causes larger and varied liquid speeds along the central axis near the narrow neck position. According to Fig. 3, it can be found that when the inner diameter of the narrow neck is less than a half-folded of the opening diameter, which is less than 90 μm in Fig. 3(c), the moving speed of the flow along the central axis increases significantly. This is mainly because the flow amount entering the micropipette in unit time is constant, given the constant moving back speed of piston of the pump. The section area at the narrow neck position reduces as the decrease of inner diameter increases at the narrow neck position, increasing the flow speed given a constant flow amount into the micropipette in unit time. Too large a flow speed at the narrow neck position can increase the cell positioning errors and increase mechanical harm to the cell after it is held by the narrow neck. Therefore, the minimum inner diameter of the narrow-neck is determined to be a 0.45-folded opening diameter, which is 100 μm here. In summary, the appropriate range of inner diameter at the narrow-necked position is determined to be the 0.5-folded inner diameter of the micropipette opening according to the above analysis and (1).

From Fig. 3, it can be observed that the flow field stabilizes at a distance of approximately 2 times the inner diameter of the micropipette. To ensure complete stabilization and account for potential variations, we conservatively selected a distance of 2.5 times the inner diameter (500 μm in our simulation). The liquid speed along the central axis becomes consistent with that of CSMs. As the aspiration force of the micropipette is generated by the flow inside the micropipette. The above similar flow at the NNM opening can provide the similar pulling force to pick the cell to that of the CSM when the narrow neck of the NNM is fabricated at a distance more than the 2.5-folded inner diameter of the micropipette from the opening. As mentioned before, the cell should be positioned as close to the opening as possible to save the liquid being injected into the new droplet during cell placement. Thus, the narrow neck position holding cell should be localized to be as close to the opening as possible, which is set as the 2.5-folded inner diameter of the micropipette from the micropipette opening.

B. NNM Fabrication Based on Heating-and-Rotation Method

Before NNM fabrications, straight micropipettes with constant inner diameter are prepared according to protocols given in Section III of the uploaded supplementary file “Supplementary file.pdf”. To fabricate a narrow neck structure inside the micropipette, the obtained CSM is vertically mounted on the microforge (Narishige, MF-900, Japan). A heating glass ball is made on the platinum wire of the microforge to heat the micropipette. With the glass ball, a heating-and-rotation method is developed to fabricate the NNM with the above-determined geometrical properties.

1) The Force Analysis of Micropipette During Heating Process: As shown in Fig. 4(a), when a vertical micropipette tip is moved close to the heating ball, the side of the micropipette close to the ball will be heated up at a higher temperature than the other side. The glass materials of the micropipette at the heating point expand vertically, exerting a vertical expanding force on the other section of the micropipette. As the temperature of the near side (to the heating ball) of the micropipette is higher than that of the far side, the expanding force at the near side F_{hc} is larger than that of the far side F_{hf}. According to Newton's Third Law, the other section of the micropipette exerts a reaction force on the glass materials at the heating point. Apparently, the reaction force at the nearside F_{hnr} is also larger than that of the far side F_{hfr} as the nearside has a higher temperature. The above reaction force squeezes the hot and soft glass materials at the heating point in the vertical direction, enlarging the thickness of the micropipette wall at the heating point [see Fig. 4(a)], shortening the length of the micropipette in the vertical direction at the heating point, and finally narrowing the inner diameter of the micropipette. Meanwhile, with a higher temperature, the glass at the near side is softer than that at the far side. Therefore, the increase in wall thickness and shortening degree of the micropipette length at the nearside are both larger than those at the far side, finally leading to the micropipette bending to the heating glass ball as shown in the second subfigure of Fig. 4(a).

The micropipette is heated after rotating around the central axis by 180°. The already bent micropipette bends in the opposite direction, which becomes straight again within a narrow neck.

2) Heating Parameters Determination Based on Heating Model: To generate the aforementioned geometrical properties of the NNM, the required heating properties of the commercial microforge need to be determined first. To achieve this, a heating model of a micropipette is developed to estimate the temperature field around the micropipette generated by the heating ball of the microforge, as shown in Fig. 4(b) and uploaded supplementary video file "Dynamic expanding process of heating field video.mp4". The detailed introduction of the heating model and the determination of heating parameters are given in Sections IV and V, respectively, of the supplementary file "Supplementary file.pdf".

3) NNM Fabrication Based on a Heating-and-Rotation Method: Based on the above work, a heat-and-rotating fabrication method is developed to generate a narrow neck inside the micropipette and keep the micropipette straight in the axial direction. As shown in Fig. 5(a), four heating points A, C, B, and D with a 90° interval from one to another are selected to fabricate the NNM. First, the glass ball heats a micropipette at A. When the micropipette is detected to be bent by 10°, the micropipette is rotated by 180° around the central axis of the micropipette to heat the opposite point B, bending the micropipette in the reverse direction to make it straight again. Then, the micropipette is rotated by 90° to heat at point C, bending the micropipette again by 10°. After that, the micropipette is then rotated by 180° to heat at point D for straightening the micropipette again. The above heating process is repeated until the inner diameter at the narrow neck position is detected to be reduced to the determined value. The reader may find more details of the above process in the uploaded supplementary video file "Heating-and-rotation method video.mp4".

During the above process, the rotation degree of the micropipette is quantified by a mark on the micropipette holder. The bending degree and inner diameter at the narrow neck of the micropipette are calculated by the image processing methods based on the online-captured microscopic images and confirmed by the operator through the angle mark in the field of view. After each two heating steps, when the micropipette becomes straight again, the inner diameter of the micropipette at the narrow-necked position is detected through image processing methods to confirm that an appropriate narrow neck has been achieved for cell holding. The detailed introduction of image processing methods for bending degree and inner diameter detection of the micropipette has been introduced in Section VI of the uploaded supplementary file "Supplementary file.pdf". Before being mounted on a micromanipulator, the NNM is finally bent by 30° using a tweezer after it becomes soft under heating at a point far away from the narrow neck (point E in Fig. 5(b)), making its tip horizontal after being mounted on the manipulator. The micropipette fabrication procedures, including heating, bending, and straightening at points A and B, are shown in Fig. 5(c)–(f).

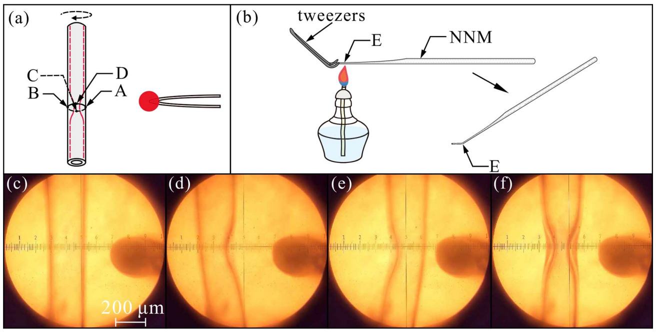

Fig. 5. The fabrication process of NNM. (a) The four heating points of the heating-and-rotation method. (b) The NNM bends 30° for mounting on the manipulator. (c)–(f) The fabrication process photos based on the heating-and-rotation method.

C. The Dynamic Model of Cell Before Held by Narrow Neck

The cell positioning process is shown in Fig. 6(a) and Fig. S9 in Section VIII of the uploaded supplementary file "Supplementary file.pdf". When using an NNM connected to a pneumatic microinjector to aspirate a target spherical cell, the piston of the pneumatic microinjector is pulled backward to generate an aspiration pressure as shown in Fig. 6(a). This aspiration pressure generates a fluid flow and produces a dragging force to move the cell. Defining the central axis of the micropipette as the X-axis direction, the dragging force F_d can be obtained as

$$F_d = m_c \ddot{x}_c \tag{2}$$

where m_c is the mass of the cell; x_c is the position of the oocyte along the X-axis direction of the NNM. According to Stokes' Law [25] and [26], the dragging force can be calculated according to

$$F_d = 6\pi\eta r_c(\dot{x}_f - \dot{x}_c)\lambda \tag{3}$$

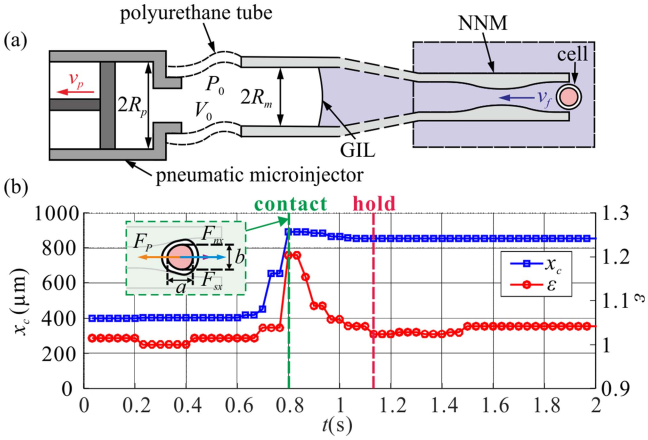

Fig. 6. Schematic diagram of cell positioning process and detected cell results. (a) Schematic of cell positioning. (b) Position and deformation curves of the cell positioning process with the force analysis in the contacting state of the cell.

TABLE I
POLYNOMIAL FITTING COEFFICIENTS FOR VELOCITY OF NNM IN $(0\,\mu\text{m}, 700\,\mu\text{m})$

NO.	D_n (μm)	a	b	c	d	R^2
1	80					0.995
2	90					0.996
3	100	0.982	0.0225	457.967	0.0405	0.998
4	110					0.996
5	120					0.995

TABLE II
POLYNOMIAL FITTING COEFFICIENTS FOR VELOCITY OF NNM IN $(700\,\mu\text{m}, 950\,\mu\text{m})$

NO.	D_n (μm)	g	h	R^2
1	80			0.995
2	90			0.996
3	100	4.221×10^5	-2.827×10^7	0.998
4	110			0.996
5	120			0.995

where r_c is the radius of the cell, which is set as 75 μm for sheep oocytes; $\dot{x}_f$ is the flow velocity of the culture medium around the cell; η is the viscosity coefficient of the culture medium. λ is a correction factor related to the relative dimensions of the inner wall radius of NNM and the radius of the cell, which can be calculated according to

$$\lambda = \frac{r_c}{r_n(x_c)} \tag{4}$$

where $r_n(x_c)$ is the inner wall radius of the NNM at the cell's position. Assuming the gas inside the gas channel between the piston and the liquid inside the micropipette is the ideal gas fulfilling the Clapeyron Equation and ignoring the temperature variation of the gas during the oocyte positioning process, the pressure variation ΔP, and the volume variation ΔV fulfill

$$P_0V_0 = (P_0 + \Delta P)(V_0 + \Delta V) \tag{5}$$

when the piston of the pneumatic microinjector moves, where P_0 and V_0 are the pressure and volume at the beginning, respectively. Changing the representation of (5) to a different way, and due to $V_0 \gg \Delta V$, we have

$$\Delta P = -P_0\frac{\Delta V}{V_0 + \Delta V} \approx -P_0\frac{\Delta V}{V_0} \tag{6}$$

For the pressure system, the gas space is enclosed by the piston and the gas-liquid interface (GLI) inside NNM. Assuming the positions of position and GLI are x_p and x_i, respectively. The change in gas volume can be obtained as

$$\Delta V = \Delta V_p - \Delta V_i = A_p\Delta x_p - A_i\Delta x_i \tag{7}$$

where ΔV_p is the change in gas volume caused by the movement of the piston; ΔV_i is the change in gas volume caused by the movement of GLI; A_p is the cross-sectional area of the channel at which the piston moves, and A_i is the cross-sectional area of the space inside NNM at the GLI position; Δx_p is the displacement of the piston, and Δx_i is the displacement of GLI inside the NNM. The value of A_p and A_i can be calculated according to

$$A_p = \pi r_p^2 \tag{8}$$

$$A_i = \pi r_i^2 \tag{9}$$

where r_p is the inner radius of the channel at the piston position, r_i is the inner radius of NNM at the GLI. Substituting (7), (8), and (9) into (6) yields

$$\dot{x}_i = \frac{V_0\dot{P}}{\pi P_0 r_i^2} + \frac{r_p^2}{r_i^2}\dot{x}_p \tag{10}$$

In the NNM, there is a relationship between the velocity at the GLI $\dot{x}_i$ and the velocity of the culture medium $\dot{x}_f$ of the cell position as

$$\dot{x}_f = f(x_c)\dot{x}_i \tag{11}$$

Substituting (3), (10), and (11) into (2) yields

$$\ddot{x}_c = \frac{6\pi\eta r_c{}^2}{m_c r_n(x_c)}\left[\left(\frac{V_0\dot{P}}{\pi P_0 r_i^2} + \frac{r_p^2}{r_i^2}\dot{x}_p\right) f\left(x_c\right) - \dot{x}_c\right]. \tag{12}$$

The expression of $f(x_c)$ is quantified according to the aforementioned microfluidics model. In the model, the mass density and viscosity coefficient of the culture medium are set to 1008.2 kg/m^3 and 1.6569 $\times 10^{-3}$ m^2/s, respectively, according to reference [27]. The geometrical properties of the micropipette are determined by the aforementioned image processing methods in Section III(B). To obtain the universal relationship, the obtained velocity data were centralized and scaled according to

$$f(x_c) = \begin{cases} \frac{a}{1+e^{-b(x_c-c)}} + d, & x_c \in (0, 700\,\mu\text{m}] \\ \left(\frac{g}{d_n} + h\right)(x_c - 700)^3 + 1, & x_c \in (700, 950\,\mu\text{m}] \end{cases} \tag{13}$$

The parameters of the fitting results are shown in Tables I, II, and Fig. S10 in Section IX in the uploaded supplementary file "Supplementary file.pdf", respectively.

D. The Dynamic Model of Cell After Held by Narrow Neck

After a cell comes into contact with the neck, the culture medium no longer flows. The generated aspiration pressure ΔP and aspiration force F_p to the cell can be obtained according to

$$F_p = \Delta P S = \Delta P \pi r_h^2 \tag{14}$$

respectively, where S is the cross-sectional area of the inner space of NNM at the position where the cell is held. In addition, the target cell is also subjected to supporting force and friction force exerted by the inner surface of the micropipette in the X-axis direction. According to Newton's Second Law, the acceleration of a cell moving along the X-axis direction can be obtained according to

$$\ddot{x}_c = \frac{F_p - F_{sx} - F_{nx}}{m_c} \tag{15}$$

where F_{sx} is the component of cellular frictional force along the X-axis direction and F_{nx} is the component of supporting force along the X-axis direction.

E. Robotic Fast Cell Positioning Process in Cell Transportation

Cell positioning controller design before and after cell holding is introduced in Section X in the supplementary file "Supplementary file.pdf". After the NNM is manually moved into the field of view, a contact detection between the micropipette and the petri dish bottom is performed to lower the micropipette tip to the petri dish bottom [28]. Then, the system automatically scans the oocyte area to conduct a global localization of oocytes through image stitching [29]. According to the localized cell positions, the cell is moved into the field of view for the cell positioning and transportation operation one by one. Based on the detected cell position and micropipette tip position, the NNM tip approaches the cell and aspirates it into its opening. During this process, the cytoplasm contour is measured online to localize the cell and calculate the cell deformation indicator. The sliding mode motion controller controls the cell motion before it is held by the narrow neck. After the cell holding is detected through the cell motion speed, the system automatically switches to the deformation controller to reduce the cell deformation indicator to a threshold value. After the positioning task is conducted, the micropipette moves out the present droplet, enters the target droplet according to its set position before the experiment, and then injects the held cell with positive pressure to finish the cell placement. The detailed cell positioning process and transportation can be found in the uploaded supplementary video file "Robotic oocyte transportation video.mp4".

IV. EXPERIMENT RESULTS

In this section, five NNMs with an inner diameter of about 200 μm and about 100 μm at the opening and narrow neck part, respectively, were fabricated to validate the repeatability of the proposed fabrication method of NNM in Section III(B).

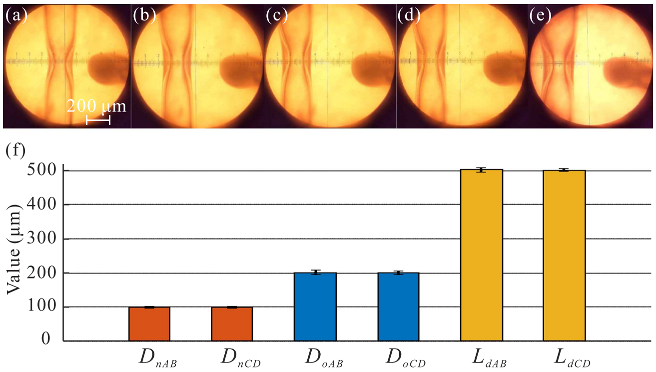

Fig. 7. Geometrical characterization of the fabricated NNMs. (a)–(e) Images of five independently fabricated NNMs, showing the consistency of the fabrication process. (f) Statistical results of the key geometrical parameters ($n = 5$ for each group): the inner diameter of the narrow neck viewed from the A-B plane (D_{nAB}) and the C-D plane (D_{nCD}), the inner diameter of the opening (D_{oAB}, D_{oCD}), and the distance from the narrow neck to the pipette opening (L_{dAB}, L_{dCD}). The small variations in these parameters demonstrate the high repeatability and precision of the proposed heating-and-rotation fabrication method. Error bars represent standard deviation.

Then, robotic positioning results of sheep oocytes in the MII stage, which usually have a diameter of 140–160 μm using the proposed system, were compared with the manual operation results using a CSM as well as an NNM to evaluate the motion control errors and cell deformation. Following the NNM fabrication protocol, we further produced thinner NNMs suitable for transporting HeLa cells, with opening and narrow neck inner diameters of 40 μm and 10 μm, respectively. These devices were used for robotic positioning of HeLa cells, and the results were compared with manual operations in terms of success rate. Finally, the viability of the oocytes and HeLa cells after a robotic positioning operation was tested to evaluate the influence of mechanical harm to the cell during the cell holding process on the cell viability.

A. Fabrication Results of NNM

The repeatability of inner diameter, section length, and distance to the opening of the narrow neck of the NNMs was tested to validate the effectiveness of the proposed heating-and-rotation method. The NNMs fabrication results ($n = 5$) are summarized in Fig. 7.

The inner diameters of each NNM at the narrow neck position between different heating point pairs were measured through mouse clicking and compared with each other to estimate the inner diameter control errors during the heating process. As shown in the left two bars in Fig. 7(f), the average inner diameter of five NNMs between the heating point A and B (denoted as D_{nAB}) and that between heating point C and D (denoted as D_{nCD}) are (98.87 $\pm$ 2.74 μm ($n = 5$) and 99.08.4 $\pm$ 2.76 μm ($n = 5$), respectively. It can be found that they are both very close to the set value (100 μm) with average error less than 1.23%, proving the effectiveness of the inner diameter control of the heating-and-rotation fabrication method of NNM. Further, it can be found that the above two values are very close to each other with an average error of less than 0.21% ($p = 0.66$, two-tailed test), proving the good consistency of inner diameter at narrow neck position around the axis direction. The above consistency indicates our method can generate a smooth and consistent inner surface of narrow neck structure around the axis direction, which is key for preventing fluidic turbulence.

Further, the inner diameter of the micropipette opening obtained from the A-B point view (denoted as D_{oAB}) and that obtained from the C-D point view (denoted as D_{oCD}) are 201.03 ± 6.45 μm ($n = 5$) and 200.94 ± 5.23 μm ($n = 5$), respectively, as shown in the central two bars in Fig. 7(f), which both are very close to the initial set value 200 μm (with average error less than 0.51%) and also close to each other. The results demonstrate that our NNM fabrication method has very limited influence on the opening size of the NNM.

Moreover, the distances from the narrow neck position to the micropipette opening of each micropipette are obtained from different views to validate the repeatability and consistency of the narrow neck position control error of our fabrication method. The average distance from narrow neck position to micropipette opening obtained from A-B point view and that obtained from C-D view are 503.31 ± 6.45 μm ($n = 5$) and 501.86 ± 4.45 μm ($n = 5$), respectively, as shown in the right two bars in Fig. 7(f). It can be found that the above two values are close to each other with an average relative difference less than 0.29% ($p = 0.28$, two-tailed test) and the variations of the above two distances are less than 1.28%, proving good repeatability and a small control error of the NNM position of our fabrication method.

B. Robotic Oocyte Positioning Results

The sheep oocytes prepared according to standard protocols [24] were selected for the robotic positioning task in cell transportation. These oocytes were first aspirated into an aspiration micropipette with an inner diameter of 200 μm and then placed into the petri dish. Then they were operated one-by-one according to procedures introduced in Section III-E. As a comparison, the oocytes were then manually positioned by an operator with more than one year of experience using the same NNM and CSM with a constant inner diameter same as the opening size of the NNM.

For cell positioning using NNM, successful cell positioning is considered to be conducted if the target oocyte is finally stuck by the narrow neck inside NNM. The final positioning error is defined as the error between the real cell position and the ideal position in the narrow neck with no cell deformation. For cell positioning with a CSM, successful cell positioning is considered to be conducted if the target cell stops at a position close to the designed position. The positioning error is defined as the distance between the final cell position and the designed position. The cell deformation degree ϵ is defined as the difference between the deformation index of the cell shown in Eq. (S10) of the supplementary file "Supplementary file.pdf". The experimental results of the above three methods are summarized in Fig. 8.

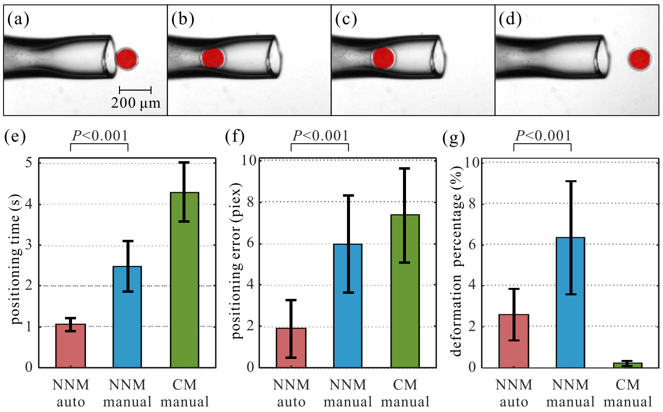

Fig. 8. Results of cell positioning experiment. (a)–(d) Cell positioning process by NNM. (e)–(g) The average operation time, positioning error, and deformation degree of the robotic method using NNM, the manual method using NNM, and the manual method using CSM.

Experimental results demonstrated our system can position the oocytes with a 100% success rate (15/15) at an average speed of 1.06 s/cell. The average positioning error and cell deformation degree are 1.89 pixels (10×, 1 pixel = 2.90 μm) and 2.59% on average, as shown in Fig. 8. The cell positioning speed is significantly faster than that reported by robotic methods based on CSMs, such as reference [22] (3.22 s/cell for oocytes), proving the effectiveness of using NNM to accelerate the cell positioning speed. The average positioning error based on NNM is similar to the current level with CSM, such as reference [21] (3pixels, 1pixel = 2.1 μm), proving that the cell positioning accuracy using NNM was similar to that of CSM.

In comparison, the manual cell positioning using a CSM only has a success rate of 81.3% (13/16). The 3 failure cases occurred when the oocytes disappeared from the CCD's field of view. Without a narrow neck to squeeze the cell, the cell deformation using a straight micropipette has the least cell deformation among the three methods (0.22%), which is mainly caused by the image processing errors. However, a lack of narrow structure to hold the cell during the cell positioning process, the average operation time of manual cell positioning using a CSM is as long as 4.30 s/cell, which is the longest among the three methods. The manual positioning errors are comparatively large, mainly due to the lack of a cell holding structure inside micropipette and accurate cell positioning methods.

In comparison to the above two methods, the manual cell positioning method using NNM operates cells with a success rate of 100% (15/15) at an average speed of 2.48 seconds/cell, which is about 233.96% slower than the robotic method. More importantly, as a lack of cell positioning controller and cell deformation controller in Section III, the average cell deformation and cell position error of the manual cell positioning using NNM are 6.34% and 5.34 pixels, which are 2.45-folded and 3.15-folded those of the robotic method, respectively.

In summary, the higher operation speed in comparison to the two other manual operation speeds proves the effectiveness of the narrow structure and integrated cell motion controller for NNM in Section III(C). Besides, the much smaller cell deformation in comparison to the manual operation results using NNM proves the effectiveness of the cell deformation controller in Section III(D).

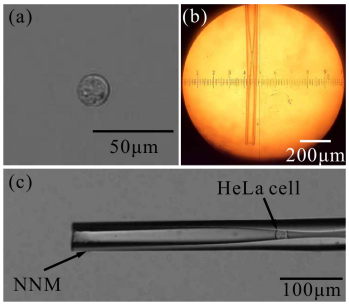

Fig. 9. Transportation of a HeLa cell using an NNM. (a) Bright-field microscopy image of a single HeLa cell in suspension. (b) CCD Image of the fabricated NNM in the microforge. (c) Optical micrograph showing the successful holding of the HeLa cell by the NNM via aspiration.

TABLE III
EXPERIMENTAL RESULTS OF HELA CELL TRANSPORTATION SUCCESS RATE

Method	Cell transportation success rate
Manual CSM	53.3% (16/30)
Manual NNM	83.3% (25/30)
Robotic NNM	**100%** (30/30)

C. Robotic HeLa Cell Positioning Results

This article also tests the capability of NNM for cell transportation from one droplet to another droplet in small-sized cells (10 μm-level scale). HeLa cells (approximately 20 μm in size) are a typical small-sized cell as shown in Fig. 9(a). According to the design principle in Section III, we achieved the fabrication of NNM for HeLa cell transportation as shown in Fig. 9(b). Due to the small size of HeLa cells and the small depth of field under high-power microscopes, HeLa cells are usually defocused during positioning, so it is difficult to segment the image and calculate the deformation of HeLa cells. This article adopts the PID control method to achieve position control of HeLa cells. Based on NNM, a single HeLa cell is positioned and held by the narrow neck of NNM, as shown in Fig. 9(c). The complete cross-droplet transportation video of a single HeLa cell can be found in the uploaded supplementary video file ”Robotic HeLa cell transportation video.mp4.

As shown in Table III, the success rate of HeLa cell transportation using robotic CSM is only 53.3%. This limited performance is primarily because the CSM lack structural constraints to stop HeLa cells. Consequently, HeLa cells are prone to be lost from the field of view, leading to positioning failure and ultimately resulting in transportation failure. In comparison, the manual NNM performed by an experienced experimenter with over 1 year of operational expertise achieved a considerably higher success rate of 83.3%. This improvement can be attributed to the narrow neck structure of the NNM, which effectively restricts the movement of HeLa cells. However, some transportation failures still occurred due to excessive pressure application, causing HeLa cells to penetrate through the constriction of narrow neck. Remarkably, the robotic NNM approach achieved a perfect success rate of 100% (30/30), enabling rapid cell transportation. The average positioning time was approximately 2.1 s ($n = 30$), significantly faster than current small-cell aspiration techniques, while the complete transportation process averaged 6 s [21].

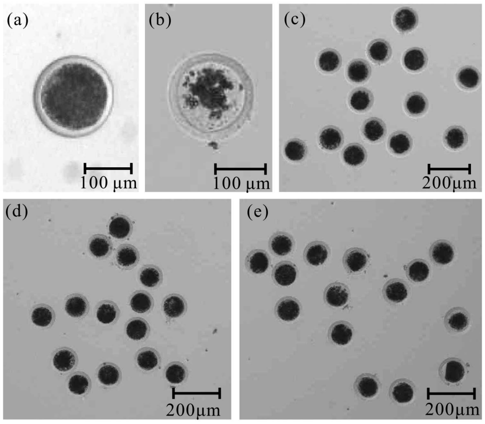

Fig. 10. Oocyte culturing results. (a)–(b) A survival oocyte after 12 hours of culture and a dead oocyte after 12 hours of culture. (c)–(e) Oocytes were cultured for 12 hours after transportation by CSM manually, NNM automatically, and NNM manually, respectively.

TABLE IV
EXPERIMENTAL RESULTS OF HELA CELL SURVIVAL RATE AFTER CULTURE

Method	Survival rate after 12 hours of culture
Manual NNM	84% (21/25)
Robotic NNM	**100% (30/30)**

D. Oocyte Culturing Results After Cell Transportation

The survival rates of the three groups of oocytes were tested after they were operated on by the aforementioned three methods, respectively, to evaluate the harm caused by the above methods to the oocyte viability.

The operated oocyte is considered to survive if an integrated cytoplasm with a clear membrane exists (see Fig. 10(a)) after 12 hours of culture. If the cytoplasm is loose or without a clear membrane (see Fig. 10(b)), it means the viability of the oocyte is damaged and the oocyte may be dead. The viability of the oocyte was also evaluated using fluorescein diacetate [30] live-cell staining as shown in Fig. S12 of the supplementary file “Supplementary file.pdf”. According to the observation results [see Fig. 10(c)], 0 of 14 oocytes was found with cytoplasm loose or without clear membrane, which proves a 100% (14/14) oocyte survival rate of oocytes operated by manual method using CSM, which is the same to that of the oocytes operated by robotic method using NNM (100%,15/15) [see Fig. 10(d)]. This can be attributed to the limited cell deformation of our robotic method with the cell deformation controller. In comparison [see Fig. 10(e)], the survival rate of manual operation using NNM is 86.7% (13/15) due to the larger cell deformation during cell positioning. The above results demonstrate that our cell positioning method has no significant damage to the cell survival rate in comparison to the manual method using a CSM.

E. HeLa Cell Culturing Results After Cell Transportation

The survival of HeLa cells was determined by the fluorescein diacetate method as shown in Fig. S13 of the supplementary file “Supplementary file.pdf”. As shown in Table IV, following manual NNM transportation, the cell viability reached 84% (21/25) after 12 hours of cultivation. This suboptimal survival rate can be attributed to the substantial momentum with which HeLa cells frequently impacted the narrow neck region during manual operation, despite the structural capability of the narrow neck to physically retain the cells. In contrast, the cell viability of the proposed robotic NNM-based transportation method reached 100% (30/30), incorporating a controller that dynamically adjusts the control output in real time, thereby optimizing the translational velocity of HeLa cells through the narrow neck. This active motion regulation minimizes mechanical impact and effectively reduces cellular damage during transportation.

V. DISCUSSION

Different from the other current cell positioning methods relying on complicated pressure control algorithms inside a CSM, this article improved the micropipette fabrication protocols and developed a narrow-necked micropipette, which uses the special narrow neck structure to hold the cell and thus "position" it forcefully. Experimental results demonstrate that the narrow neck can stop a fast-moving cell immediately by force, significantly accelerating the positioning process. Meanwhile, the holding of the cell may generate cell deformation and cause mechanical stimulation to the cell. Through the designed deformation controller, the aspiration pressure is adjusted after the cell is held to reduce the cell deformation and potential mechanical harm to the cell. Besides, the cell survival testing results also proved the proposed cell positioning method has no significant damage to cell viability in comparison to the traditional positioning method using a CSM.

The target cells in this study were porcine oocytes (diameter $\sim$150 μm) and HeLa cells (diameter $\sim$20 μm). The NNM achieved high success rates (100%) and rapid transport times (1.06 s for porcine oocytes and 2.1 s for HeLa cells), demonstrating its capability for cross-scale cell transportation across a wide size range ($\sim$20 to $\sim$150 μm). Due to the power limitation of the microforge used in this article, it is a challenging task to fabricate a narrow structure inside a micropipette with an opening diameter larger than 500 μm. To quickly position the giant cell larger than the above thresholding value, such as zebra fish embryos, new fabrication of NNM should be developed. Our previously developed bilayer micropipette [24] may be an ideal tool for fast positioning of the giant cells.

It is worth noting that the influences of the cell are ignored in the computational microfluidic model, as shown in Fig. 3(a) and (b). Fortunately, the NNM with geometrical properties determined by the computational model still has a better performance in cell transportation than CSM, which proves the above simplification may have limited negative influences for cell positioning control. Besides, our system is only able to operate one cell at a time due to only one NNM is mounted in the system. In the future, the narrow neck structure can be realized in the microfluidic channel, which can be assembled into a parallel system with multiple channels in a chip. In that way, multiple cells are expected to be positioned and transported in parallel.

The cell dynamics model derived in this article is based on the Stokes drag formulation, which introduces certain errors in confined flow fields. However, the core advantage of the sliding mode controller designed in this article lies in its inherent robustness to variations in model parameters and unmodeled dynamics. Consequently, even with some model errors, the system's asymptotic stability remains assured, ultimately validated by experimental results.

VI. CONCLUSION

This article developed a robotic fast cell positioning method based on a self-made NNM. Dynamic models of cells before and after being held by a narrow neck were carried out through fluid dynamics simulation and force analysis, respectively. Based on that, a sliding mode controller and a deformation controller combined are designed for motion control and cell deformation control, respectively. The experimental results demonstrated that the method positions the cells at the narrow neck position in an average of 1.06 seconds, which has a double throughput of than the traditional methods, with a 100% operation success rate, a positioning error of 1.89 pixels and 2.59% cell deformation degree on average, and no observable harm to the survival rate of oocytes. Furthermore, cross-droplet transportation of HeLa cells was successfully achieved, with an average aspirating time of 2.1 s, a 100% success rate, and 100% cell viability after 12 hours of cultivation. With the above advantages, the proposed robotic cell positioning method is highly expected to improve cell transportation efficiency in biological applications.

REFERENCES

[1] S. Miao et al., "Microfluidics-enabled robotic system for embryo vitrification with real-time observation: Design, method, and evaluation," *IEEE/ASME Trans. Mechatron.*, vol. 29, no. 1, pp. 179–189, Feb. 2024.

[2] Z. Zhang et al., "Robotic pick-and-place of multiple embryos for vitrification," *IEEE Robot. Autom. Lett.*, vol. 2, no. 2, pp. 570–576, Apr. 2017.

[3] X. Shi, W. Tan, Y. Lu, W. Cao, and G. Zhu, "A needle tip CCEA microfluidic device based on enhanced dean flow for cell washing," *Microsyst. Nanoeng.*, vol. 7, no. 1, 2021, Art. no. 81.

[4] M. Xie, Y. Wang, G. Feng, and D. Sun, "Automated pairing manipulation of biological cells with a robot-tweezers manipulation system," *IEEE/ASME Trans. Mechatron.*, vol. 20, no. 5, pp. 2242–2251, Oct. 2015.

[5] C. Jiang and J. K. Mills, "Planar cell orientation control system using a rotating electric field," *IEEE/ASME Trans. Mechatron.*, vol. 20, no. 5, pp. 2350–2358, Oct. 2015.

[6] L. Wen and F. Tang, "Recent advances in single-cell sequencing technologies," *Precis. Clin. Med.*, vol. 5, no. 1, 2022, Art. no. pbac002.

[7] X. Liu et al., "Noncontact 3-D orientation control at microscale: Hydrodynamic out-of-plane rotation and in-plane rotation by compacted rotational stage," *IEEE/ASME Trans. Mechatron.*, vol. 27, no. 6, pp. 4807–4818, Dec. 2022.

[8] G. Shan et al., "Robotic blastocyst biopsy," *IEEE/ASME Trans. Mechatron.*, vol. 28, no. 3, pp. 1372–1383, Jun. 2023.

[9] A. K. Dutta, J.-B. Alberge, R. Sklavenitis-Pistofidis, E. D. Lightbody, G. Getz, and I. M. Ghobrial, "Single-cell profiling of tumour evolution in multiple myeloma—Opportunities for precision medicine," *Nat. Rev. Clin. Oncol.*, vol. 19, no. 4, pp. 223–236, 2022.

[10] S. Kang, X. Yang, Y. Li, H. Wu, and T. Li, "A fractional viscoelastic mechanical model for speed optimization of robotic cell microinjection," *IEEE/ASME Trans. Mechatron.*, vol. 29, no. 6, pp. 4514–4525, Dec. 2024.

[11] S. Hu, S. Chen, S. Chen, G. Xu, and D. Sun, “Automated transportation of multiple cell types using a robot-aided cell manipulation system with holographic optical tweezers,” *IEEE/ASME Trans. Mechatron.*, vol. 22, no. 2, pp. 804–814, Apr. 2017.

[12] D. Liu et al., “All-purpose magnetic micromanipulation system with two modes: Chopstick-like two-finger microhand and hydrodynamic tweezer,” *IEEE/ASME Trans. Mechatron.*, vol. 27, no. 3, pp. 1582–1593, Jun. 2022.

[13] H. Yang, X. Li, X. Li, L. Sun, and D. Sun, “A virtual-assisted controller for biological cell transportation in a dynamic environment with variable field of view,” *IEEE/ASME Trans. Mechatron.*, vol. 25, no. 3, pp. 1255–1265, Jun. 2020.

[14] S. Sart, G. Ronteix, S. Jain, G. Amselem, and C. N. Baroud, “Cell culture in microfluidic droplets,” *Chem. Rev.*, vol. 122, no. 7, pp. 7061–7096, 2022.

[15] A. Shakoor et al., “Achieving automated organelle biopsy on small single cells using a cell surgery robotic system,” *IEEE Trans. Biomed. Eng.*, vol. 66, no. 8, pp. 2210–2222, Aug. 2019.

[16] A. Lefevre, V. Gauthier, M. Gauthier, and A. Bolopion, “Closed-loop control of particles based on dielectrophoretic actuation,” *IEEE/ASME Trans. Mechatron.*, vol. 27, no. 6, pp. 4764–4773, Dec. 2022.

[17] T. Michálek, A. Bolopion, Z. Hurák, and M. Gauthier, “Electrorotation of arbitrarily shaped micro-objects: Modeling and experiments,” *IEEE/ASME Trans. Mechatron.*, vol. 25, no. 2, pp. 828–836, Apr. 2020.

[18] B. Ahmad, A. Barbot, G. Ulliac, and A. Bolopion, “Remotely actuated optothermal robotic microjoints based on spiral bimaterial design,” *IEEE/ASME Trans. Mechatron.*, vol. 27, no. 5, pp. 4090–4100, Oct. 2022.

[19] H. Gu, R. Zhai, C. Yue, Y. Sun, and C. Dai, “Automated sperm immobilization with compensation for sperm intrinsic and fluid flow-induced movements,” *IEEE/ASME Trans. Mechatron.*, vol. 30, no. 6, pp. 6198–6208, Dec. 2025.

[20] X. P. Zhang, C. Leung, Z. Lu, N. Esfandiari, R. F. Casper, and Y. Sun, “Controlled aspiration and positioning of biological cells in a micropipette,” *IEEE Trans. Biomed. Eng.*, vol. 59, no. 4, pp. 1032–1040, Apr. 2012.

[21] G. Shan, Z. Zhang, C. Dai, X. Wang, L.-T. Chu, and Y. Sun, “Model-based robotic cell aspiration: Tackling nonlinear dynamics and varying cell sizes,” *IEEE Robot. Autom. Lett.*, vol. 5, no. 1, pp. 173–178, Jan. 2020.

[22] X. Zhao et al., “Aspirating cell into orifice of micropipette for precise cell transportation using micropipette,” *IEEE Trans. Autom. Sci. Eng.*, vol. 21, no. 1, pp. 181–191, Jan. 2024.

[23] R. Li et al., “Precise robotic picking up of polar body for biopsy application,” *IEEE Trans. Autom. Sci. Eng.*, vol. 22, pp. 5895–5905, 2025.

[24] J. Qiu et al., “Robotic microscopic vision-free cell transportation based on pressure variation model inside bilayer micropipette,” *IEEE Trans. Autom. Sci. Eng.*, vol. 22, pp. 4134–4144, 2025.

[25] M. Maxey and B. Patel, “Localized force representations for particles sedimenting in stokes flow,” *Int. J. Multiphase Flow*, vol. 27, no. 9, pp. 1603–1626, 2001.

[26] J. Happel and H. Brenner, *Low Reynolds Number Hydrodynamics: With Special Applications to Particulate Media*. vol. 1., Berlin: Springer, 2012.

[27] Q. Zhao, B. Shirinzadeh, M. Cui, M. Sun, and X. Zhao, “A simple weighing method for spherical cells,” *J. Lab. Autom*, vol. 20, no. 4, pp. 471–480, 2015.

[28] W. Wang, X. Liu, and Y. Sun, “Contact detection in microrobotic manipulation,” *Int. J. Robot. Res.*, vol. 26, no. 8, pp. 821–828, 2007.

[29] Q. Zhao, M. Cui, C. Zhang, J. Yu, M. Sun, and X. Zhao, “Robotic enucleation for oocytes,” in *Proc. 9th IEEE NEMS*, 2014, pp. 23–27.

[30] H. Gong et al., “Robust out-of-plane rotation of biological cells based on polar body orientation prediction,” *IEEE/ASME Trans. Mechatron.*, vol. 30, no. 6, pp. 5497–5507, Dec. 2025.

Shaojie Fu received the B.Eng. degree in automation from the Taiyuan University of Technology, Taiyuan, China, in 2023. He is currently working toward the master’s degree in artificial intelligence with the College of Artificial Intelligence, Nankai University, Tianjin, China.

His research interests include micromanipulators and microsystems.

Jinyu Qiu received the B.Eng. degree in automation from the Taiyuan University of Technology, Taiyuan, China, in 2019. He is currently working toward the Ph.D. degree in control science and engineering with the College of Artificial Intelligence, Nankai University, Tianjin, China.

From 2022 to 2023, he was a Visiting Ph.D. Student with Imperial College London, London, U.K. His research interests include robotic patch clamp systems, cell micromanipulation, and microsystems.

Ruimin Li received the B.Eng. degree in intelligence science and technology from the Hebei University of Technology, Tianjin, China, in 2022. She is currently working toward the Ph.D. degree in control science and engineering with Nankai University, Tianjin, China.

Her research interests include robotic patch clamp systems, micromanipulators, and microsystems.

Biting Ma received the bachelor’s degree in intelligent medical engineering from Nankai University, Tianjin, China, in 2023 where she is currently working toward the master’s degree in control science and engineering with the College of Artificial Intelligence.

Her research interests include robotic dual-arm patch clamp systems, micromanipulators, and microsystems.

Mengya Liu received the M.Eng. degree in electronic information from Tiangong University, Tianjin, China, in 2024. She is currently working toward the Ph.D. degree in control engineering with the College of Artificial Intelligence, Nankai University, Tianjin.

Her research interests include micro-nano manipulation, cell micromanipulation, and microsystems.

Hao Chen received the B.S. degree from Jiangnan University, Wuxi, China, in 2022, and the M.S. degree from the Qilu University of Technology (Shandong Academy of Sciences), Shandong, China, in 2024. He is currently working toward the Ph.D. degree in control science and engineering with the School of Artificial Intelligence, Nankai University, Tianjin, China.

His research interests include flexible strain sensors and microelectrode arrays in brain science.

Mingzhu Sun (Member, IEEE) received the B.S. degree in computer science and technology, the M.S. degree in computer application, and the Ph.D. degree in control theory and control engineering from Nankai University, Tianjin, China, in 2003, 2006, and 2009, respectively.

In 2009, she joined the Faculty of Nankai University, where she is currently a Professor and the Deputy Director of the Institute of Robotics and Automatic Information System. Her research interests include micromanipulation, image processing, and computer vision.

Xin Zhao (Member, IEEE) received the B.S. degree in control theory and control engineering from Nankai University, Tianjin, China, in 1991, the M.S. degree in control theory and control engineering from the Shenyang Institute of Automation, CAS, Shenyang, China, in 1994, and the Ph.D. degree in control theory and control engineering from Nankai University, in 1997.

In 1997, he joined Nankai University, where he is currently a Professor and the Dean of the College of Artificial Intelligence. His research interests include micromanipulation, microsystems, and mathematical biology.

Qili Zhao (Member, IEEE) received the Ph.D. degree in control theory and control engineering from Nankai University, Tianjin, China, in 2014.

From 2014 to 2015, he was a Postdoctoral Researcher with the Robotics and Mechatronics Research Laboratory, Department of Mechanical and Aerospace Engineering, Monash University, Melbourne, VIC, Australia, and from 2015 to 2018, a Postdoctoral Fellow with the Advanced Micro and Nanosystems Laboratory, Department of Mechanical and Industrial Engineering, University of Toronto, Toronto, ON, Canada. He is currently an Associate Professor with the College of Artificial Intelligence, Nankai University. His current research interests include robotic patch clamp, robotic cell manipulation, and robotic cell measurement.